

Boosting Electrochemical Performance of FeP₂ Anodes for Li-Ion Batteries by a Mxene Modification Strategy

Chenyi Yang, Wende Bai, Zhe Gong,* Zhuo Li, Pengfei Wang,* Mingdong Zhou, and Kai Zhu*

Lithium-ion batteries, characterized by high energy density, are a promising energy storage device. However, the poorly matched kinetics of the electrochemical reaction between the anode and cathode of lithium-ion batteries make the search for anode materials with high ion-electron transfer efficiency an urgent task. In this work, Fe³⁺ is introduced through the branch-end negative charge of Ti₃C₂ to construct a 3D Fe³⁺/Ti₃C₂ spatial network structure, and then FeP₂@Ti₃C₂ is formed by hydrothermal and low-temperature phosphatization. The 2D nanosheet structure in FeP₂@Ti₃C₂ provides more storage sites for Li⁺ ions, and the

Ti₃C₂ contributes to the enhancement of the electrical conductivity of the transition metal phosphide. Because the electronic structure of transition metal phosphides is similar to that of metals, rapid electron transfer and ion diffusion channels are formed in the longitudinal direction between layers. The FeP₂@Ti₃C₂ composite material still has a specific capacity of 1194 mAh g⁻¹ after 1000 cycles at 1000 mA g⁻¹ current density. This article provides guidance for the design of 2D materials, and FeP₂@Ti₃C₂ composites have great potential for next-generation energy storage with their unique structure and excellent electrochemical properties.

1. Introduction

Since entering the 21st century, energy has been a huge problem that people need to solve. 2022, the global primary energy consumption to reach 604.04 EJ,^[1–3] the traditional energy to meet the needs of today's society, so the search for a new type of environmentally friendly energy has always been a major issue in the scientific community. 1991, the Sony Corporation for the first time to use the commercial lithium batteries, because of its high

energy and small size characteristics and attracted much attention.^[4–6] However, due to the safety hazards of traditional graphite anode lithium batteries,^[7,8] as well as the high cost of the defects, so we need to find a new lithium battery anode material.

Transition metal phosphides have attracted much attention due to their abundant electrochemical active sites, high electrical conductivity, and thermal and structural stability.^[9–11] As the most abundant and inexpensive transition metal element, due to its nontoxic nature and low cost, various stoichiometric compositions of iron phosphides, such as FeP, Fe₂P, and FeP₄, have been extensively studied and applied to energy storage devices due to their different nanostructures and hence different electrochemical properties.^[12–14] Veluri's team synthesized a low-phosphorus iron phosphide by using a two-step strategy, viz., FeP. The material showed a stable cycling specific capacity of 622 mAh g⁻¹ and a capacity retention of 53.7% in a half-battery configuration.^[15] Jiang's team synthesized phosphorus-rich FeP₂/carbon nanotube nanocomposites using pyrolysis process and considered as a novel anode material for lithium-ion batteries.^[16] Zhu's team doped rGO in FeP@C matrix (FeP@C/rGO) was doped with rGO, which significantly increased the reversible specific capacity. The negligible capacity decay observed even after 500 cycles was attributed to the separation of the electrode layer on the electrolyte surface.^[17] Other FeP/C composites, such as nanorod-shaped FeP@C, MOF-derived shuttle hollow and porous carbon-coated FeP (FeP@C), FeP onion-like composites, and FeP@rGO, have also been used as anode materials for Li-ion batteries.^[18–20] At low current densities, the maximum specific capacities of the above materials were 480 mAh g⁻¹ (after 200 cycles), 902.4 mAh g⁻¹ (after 100 cycles), 915 mAh g⁻¹ (after 500 cycles), and 460 mAh g⁻¹ (after 400 cycles), respectively. The theoretical specific capacity of FeP₂ is even higher than 1365 mAh g⁻¹, which is much higher than that of conventional graphite anode

C. Yang, Z. Gong, M. Zhou
College of Chemical Engineering
Shenyang University of Chemical Technology
Shenyang 110142, P. R. China
E-mail: zgong@syuct.edu.cn

W. Bai, Z. Li, K. Zhu
Key Laboratory of Superlight Materials and Surface Technology of Ministry of Education
College of Materials Science and Chemical Engineering
Harbin Engineering University
Harbin 150001, P. R. China
E-mail: kzhu@hrbeu.edu.cn

W. Bai
Jiangsu Zenergy Battery Technologies Group Co. Ltd.
Suzhou 341000, P. R. China

Z. Li
School of Chemical Sciences
University of Auckland
Auckland 1010, New Zealand

P. Wang
School of Environmental and Chemical Engineering
Shenyang University of Technology
Shenyang 110870, P. R. China
E-mail: wangpengfei@sut.edu.cn

 Supporting information for this article is available on the WWW under <https://doi.org/10.1002/batt.202500509>

(372 mAh g⁻¹). It is a kind of lithium-ion battery anode material with development potential. However, the conductivity of phosphorus–iron compounds is poor, which is accompanied by the volume expansion of electrodes during charging and discharging.

In 2011, a series of 2D layered materials called MXene was discovered at Drexel University by exfoliating the MAX phase in hydrofluoric acid (HF).^[21] The 2D and metallic properties of this material endow it with excellent properties such as conductivity and hydrophilicity, and the huge specific surface area provides a vast space for lithium ion embedding. Therefore, MXenes have received considerable attention in energy conversion and storage technologies.^[22] Of the more than 100 known MXenes variants, Ti₃C₂T_x MXene is the most widely studied because of its excellent pseudocapacitive properties and potential for large-scale applications in LIB and LIC.^[23–28] Chen's team^[29] prepared a fiber hydroxylated Ti₃C₂/CNTs (h-Ti₃C₂/CNTs) composite with abundant natrophilic sites, good thermal conductivity, and fast ion/electron transfer kinetics. LiF and hydrochloric acid-corroded Ti₃C₂T_x MXene's terminal groups generally contain –F groups, which is unfavorable for the transport of electrolyte ions. Controlling the type and content of the end functional groups by replacing or eliminating highly electronegative ions through surface modification is a promising strategy.^[30–33] Fan's team^[34] reported a n-butyllithium treatment to change the –F and –OH end groups on Ti₃C₂T_x MXene into –O groups and that n-butyllithium-treated Ti₃C₂T_x MXene showed good performance in pseudocapacitors. Based on the above research, the rich functional groups and 2D properties of MXene are conducive to its combination with other materials to construct specific structures.

In this work, a novel 2D Ti₃C₂ material was employed as the substrate. Leveraging the negatively charged terminal groups of Ti₃C₂, Fe³⁺ cations were introduced through electrostatic attraction, leading to the formation of a 3D Fe³⁺/Ti₃C₂ network structure. Subsequently, an iron-based oxyhydroxide composite precursor was synthesized via a hydrothermal reaction, and

the final material, FeP₂@Ti₃C₂, was obtained after a low-temperature phosphorization treatment. The Ti₃C₂ network serves to confine the volume expansion of the transition metal phosphide and enhances the electrical conductivity, which is typically limited in iron-based phosphides. Furthermore, the incorporation of iron phosphide mitigates the inherent restacking issue of 2D materials, suppresses the aggregation of MXene layers, and improves interlayer ion transport efficiency. Furthermore, the theoretical specific capacity of FeP₂ (1365 mAh g⁻¹) is significantly higher than those of traditional Co- and Ni-based materials, such as LiCoO₂ (272 mAh g⁻¹) and LiNiO₂ (220 mAh g⁻¹).^[35,36] Finally, the composite was used as the anode material of lithium-ion batteries, and its electrochemical properties were investigated. To demonstrate the performance advantages of this work, we have sorted out the properties of electrode materials in other related work. The comparison result of specific capacity is shown in Figure S1, Supporting Information. At the current density of 100 mA g⁻¹, FeP₂@Ti₃C₂ has obvious capacity advantage.^[37–45] We also compared the performance with other common carbon-based and MXene-based materials, and summarized the results in Table S1, Supporting Information.^[46–55] Compared to conventional synthesis methods, our approach is more straightforward and requires less stringent processing conditions. Furthermore, the resulting FeP₂@Ti₃C₂ composite demonstrates excellent capacity and a longer cycle life across various current densities when benchmarked against the materials listed in Table S1, Supporting Information. This work provides an effective insight for improving the stability of metal phosphide.

2. Results and Discussion

FeP₂ and FeP₂@Ti₃C₂ were prepared by hydrothermal and low-temperature phosphatization methods. The preparation process of FeP₂@Ti₃C₂ was shown in Figure 1a. FeP₂ particles were

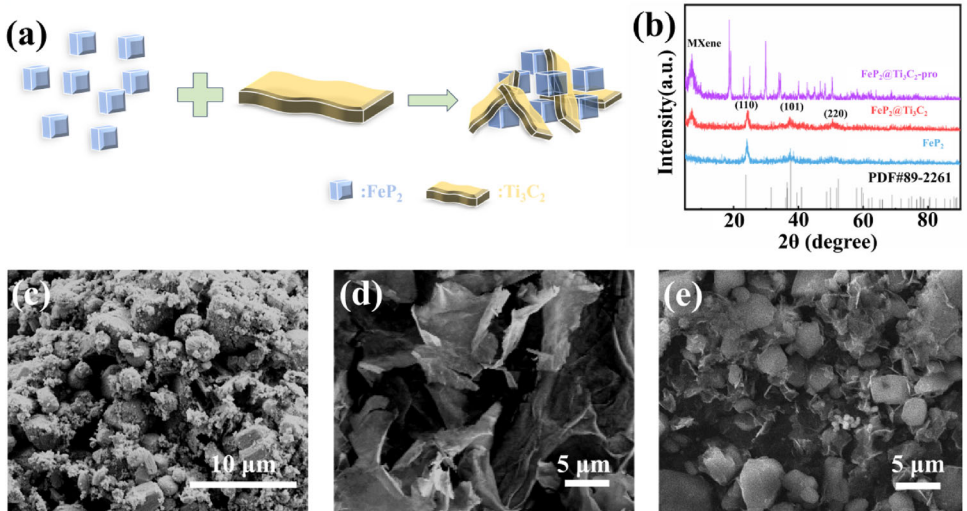


Figure 1. a) Illustration of FeP₂ preparation process. b) XRD patterns of FeP₂@Ti₃C₂-pro, FeP₂@Ti₃C₂, and FeP₂. SEM images of c) FeP₂, d) Ti₃C₂, and e) FeP₂@Ti₃C₂.

dispersed in the solution and combined with Ti_3C_2 , which had a layered structure. FeP_2 particles are uniformly distributed on the surface of Ti_3C_2 to get $\text{FeP}_2@\text{Ti}_3\text{C}_2$. To study the optimal dosage of MXene, 25, 50, and 75 mg of MXene were weighed, respectively, to prepare $\text{FeP}_2@\text{Ti}_3\text{C}_2$. The $\text{Li}||\text{FeP}_2@\text{Ti}_3\text{C}_2$ battery was assembled for long cycle testing at 1000 mA g^{-1} (Figure S2, Supporting Information). The cycle performance shows that the electrode material prepared by adding 50 mg of MXene has the best stability and specific capacity. As shown in Figure 1b, the peak patterns of the materials FeP_2 and $\text{FeP}_2@\text{Ti}_3\text{C}_2$ all corresponded to the FeP_2 standard card (PDF #89–2261), which proved that the composites were successfully prepared by hydrothermal reaction and low-temperature phosphatization. The characteristic peaks in the X-ray diffraction (XRD) pattern located at 23.8° , 37.6° , and 48.2° were related to the (110), (101), and (220) crystal planes of FeP_2 .^[56] In the XRD pattern of $\text{FeP}_2@\text{Ti}_3\text{C}_2$, the characteristic peak observed at 6.2° corresponds to the (002) plane of MXene.^[57] The presence of this distinctive MXene peak in both the precursor, $\text{FeP}_2@\text{Ti}_3\text{C}_2$ -pro and the final composite $\text{FeP}_2@\text{Ti}_3\text{C}_2$, indicates that the layered structure of Ti_3C_2 was successfully preserved throughout the hydrothermal reaction and the subsequent phosphorization process. Figure 1c showed the scanning electron microscope (SEM) images of FeP_2 , and the prepared FeP_2 showed an overall lumpy morphology, with the overall size ranging from 1 to $5 \mu\text{m}$. It could be seen that FeP_2 was stacked together and the surface was uneven, and there were a large number of FeP_2 microparticles. Generally speaking, during the embedding process of lithium ions, volume expansion occurred and larger blocks were prone to internal stresses due to volume expansion, which lead to the pulverization of FeP_2 , and thus lead to poor cycling performance. SEM tests were carried out on Ti_3C_2 (Figure 1d), and it was found that after etching and ultrasonic stripping, a clear lamellar structure of Ti_3C_2 could be observed, and the lamellar layer was thin, which showed 2D material characteristics, indicating that the use of LiF and HCl as the etching agent can be used to etch off the Al layer successfully, and then after ultrasonic stripping could be obtained after the Ti_3C_2 . In contrast, SEM test result showed that $\text{FeP}_2@\text{Ti}_3\text{C}_2$ had

a bulk structure (Figure 1e), and the surface of the bulk FeP_2 became smooth after the introduction of Ti_3C_2 , and the stacking phenomenon was alleviated, and the FeP_2 wrapped by the substrate material. The Ti_3C_2 carried negative groups such as $-\text{F}$, $-\text{OH}$, etc., and the divalent metal cations were attracted to form a honeycomb-like substrate with each other because of the positive and negative charges, crosslinked honeycomb substrate structure. The spatial network structure constructed by using the negatively charged nature of Ti_3C_2 branch ends could well separate the FeP_2 bulk structure, which not only could well avoid the stacking during the material growth process, but also could make use of the good electrical conductivity of Ti_3C_2 to make up for the disadvantage of the poor electrical conductivity of FeP_2 . The composite structure could further enhance the specific surface area of the material and shorten the distance that Li^+ passes through in the shuttle. In addition, this structure could enhance the electrical conductivity and inhibited the volume change during the Li^+ embedding and detachment process.

Transmission electron microscopy (TEM) tests were performed on $\text{FeP}_2@\text{Ti}_3\text{C}_2$ and the results were shown in Figure 2. The polyhedral structure of $\text{FeP}_2@\text{Ti}_3\text{C}_2$ was completely retained in the titanium carbide skeleton after low-temperature phosphatizing treatment. The FeP_2 nanoparticles were simultaneously grown on the titanium carbide skeleton, and the presence of the carbon skeleton could sufficiently inhibit the volume expansion during the electrochemical process and the FeP_2 nanoparticles were uniformly distributed. The retention of Ti_3C_2 as a substrate material facilitated the electron transfer throughout the composite. As shown in the Figure, FeP_2 was anchored on the Ti_3C_2 sheets to form a complete conductive network. Figure 2a,b showed that FeP_2 with a bulk structure was assembled from FeP_2 nanoparticles in the polycrystalline state, and the polycrystalline material mitigates the volume change of the material. The TEM results, presented in Figure 2c, show lattice fringes with spacings of 0.37 and 0.24 nm, which correspond to the (110) and (101) crystal planes of FeP_2 , respectively. These findings are in good agreement with the XRD results and confirm the presence of the FeP_2 crystal phase.^[58] In addition, the distribution

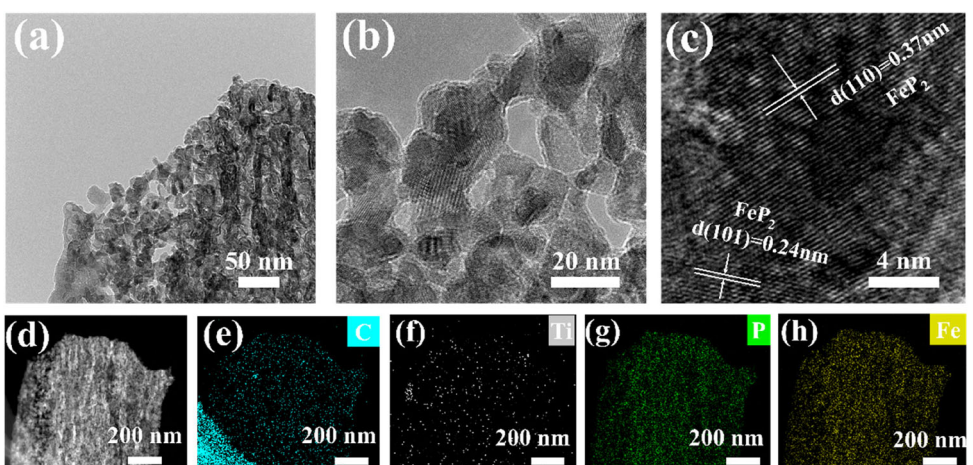


Figure 2. a,b) TEM images of $\text{FeP}_2@\text{Ti}_3\text{C}_2$. c) HRTEM image of $\text{FeP}_2@\text{Ti}_3\text{C}_2$. d–h) EDS mapping images of $\text{FeP}_2@\text{Ti}_3\text{C}_2$.

of each element in the composite was further illustrated by elemental mapping. The scanning TEM images and the corresponding elemental mapping images of C, Ti, P, and Fe are shown in Figure 2d–h, and the elements of Fe, P, C, and Ti were uniformly distributed throughout $\text{FeP}_2@\text{Ti}_3\text{C}_2$.

In order to investigate the valence structures and compositions of various elements in $\text{FeP}_2@\text{Ti}_3\text{C}_2$, X-ray photoelectron spectroscopy (XPS) tests were performed on $\text{FeP}_2@\text{Ti}_3\text{C}_2$. The result of XPS on Fe was shown in the Figure 3a, the peaks located at 720.5 and 706.8 eV were attributed to the Fe–P bond in FeP_2 , and the peaks at 729 and 714.5 eV were the Fe $2p_{3/2}$ and Fe $2p_{1/2}$ of FeP_2 . The peaks located at 724.8 and 701 eV were attributed to the Fe $2p_{3/2}$ and Fe $2p_{1/2}$ of Fe^{3+} . The peak located at 719.2 eV was attributed to the oxidation of FeP_2 by exposure to air. For the XPS result of P $2p$ (Figure 3b), the peak at 133.6 eV was attributed to P–O by the oxidation of FeP_2 because of long term exposure to air. The peak at 128.9 eV was attributed to the P–Fe bond in FeP_2 obtained by phosphorylation and the peak located at 130.0 eV was the P–C bond which formed with C of Ti_3C_2 in the process of phosphorylation. The peak located at 281.8 eV was the C–Ti bond in the substrate material Ti_3C_2 , which was seen in the XPS result of C (Figure 3c). The other peaks located at 284.8, 285.2, and 289.1 eV were attributed to C–C, C–O, and O=C=O bonds. Figure 3d showed the peaks of Ti $2p$ located at 455.1 eV ($2p_{1/2}$) and 461.6 eV ($2p_{3/2}$) were attributed to the Ti–C bonding in the substrate material. The peak at 456.1 eV was attributed to Ti^{2+} and peak at 464.3 eV was attributed to Ti^{3+} . The characteristic peaks at 458.6 and 464.9 eV were due to the oxidization of Ti_3C_2 to TiO_2 when exposed to air. The results further identified the prepared material as $\text{FeP}_2@\text{Ti}_3\text{C}_2$.

Figure 4a showed $\text{FeP}_2@\text{Ti}_3\text{C}_2$ at 0.001–3.0 V range with a sweep rate of 0.5 mV s⁻¹ for the first three cycles of cyclic voltammetry (CV) test. It could be seen that a cathodic reduction peak appears in the first cycle since around 0.95 V, which was the result of the decomposition and reduction of the electrolyte on the

surface of $\text{FeP}_2@\text{Ti}_3\text{C}_2$ into a SEI film with irreversible phase transition. The appearance of a reduction peak near 0.6 V was caused by the gradual embedding of Li^+ into the $\text{FeP}_2@\text{Ti}_3\text{C}_2$ interlayer. In contrast, during the first cathodic cycling of FeP_2 (Figure S3, Supporting Information), the FeP_2 electrode showed peaks at multiple locations, which was an indication of the formation of a solid electrolyte film on the surface of the material and the decomposition of part of the electrolyte during the first cycling process. The reduction peak at around 0.9 V during the first cycle of voltammetric cathodic process was the formation of solid electrolyte film on the surface of FeP_2 by the electrolyte and its reaction with Li^+ , while the reduction peak at around 0.3 V was the embedding of Li^+ into the interior of FeP_2 . The existence of solid electrolyte film also led to the loss of reversible specific capacity in the next cycle. The position of the reduction peak was shifted to 1.1 V in the second and third cycles, while the position of the peak of $\text{FeP}_2@\text{Ti}_3\text{C}_2$ was almost unchanged in the second and third cycles. The result showed reproducibility of the cycle curves was good, which indicates that $\text{FeP}_2@\text{Ti}_3\text{C}_2$ had a relatively good stability and provided a good basis for the electrochemical multiplication of $\text{FeP}_2@\text{Ti}_3\text{C}_2$. Ti_3C_2 electrochemical multiplicity performance enhancement. Figure 4b showed the first three charge/discharge curves of $\text{FeP}_2@\text{Ti}_3\text{C}_2$, and a discharge plateau was seen at 1.5 V. The result coincided with the peak position of the first discharge of the CV performance curve, and the material initial Coulombic efficiency was 73.3%, which was superior to that of FeP_2 with a first-turn coulombic efficiency of 67.5% (Figure S4, Supporting Information). It proved that the composite by introducing Ti_3C_2 enhanced the stability and electrochemical initial coulombic efficiency. Figure 4c showed the rate performance curves of $\text{FeP}_2@\text{Ti}_3\text{C}_2$ with specific capacities of 1018, 920, 823, 710, 501, and 340 mA h g⁻¹ at current densities ranging from 100 to 2000 mA g⁻¹. When the current densities came back to 100 mA g⁻¹, the specific capacity was 986 mA h g⁻¹, which was similar to the average specific capacity under current density of 100 mA g⁻¹ at the beginning of the cycle. The result showed that $\text{FeP}_2@\text{Ti}_3\text{C}_2$ had excellent performance in terms of cyclic reversibility.

Figure 5a showed the electrochemical impedance profiles of FeP_2 and $\text{FeP}_2@\text{Ti}_3\text{C}_2$, and it was seen that $\text{FeP}_2@\text{Ti}_3\text{C}_2$ (51 Ω) exhibited the better electrochemical performance than FeP_2 (227 Ω). The decrease in impedance was due to the introduction of Ti_3C_2 , there was a better contact between the electrolyte and the material, and the formation of stable electrode–electrolyte interfaces. It also illustrated the fact that introducing the Ti_3C_2 could significantly improve the electrical conductivity of the composites. We performed equivalent circuit fitting analysis on the electrochemical impedance spectroscopy (EIS) results, as shown in Figure 5a. The constant phase element (CPE) accounts for the roughness of the electrode surface. R_{ct} represents the charge transfer resistance, while R_Ω corresponds to the combined electrolyte and electrode resistance. The double-layer capacitance, C_{dl} , suggests the presence of a high number of active sites on the electrode surface.^[59,60] The equivalent circuit fitting results confirm the presence of a C_{dl} component in $\text{FeP}_2@\text{Ti}_3\text{C}_2$, indicating that the incorporation of Ti_3C_2 effectively increases the

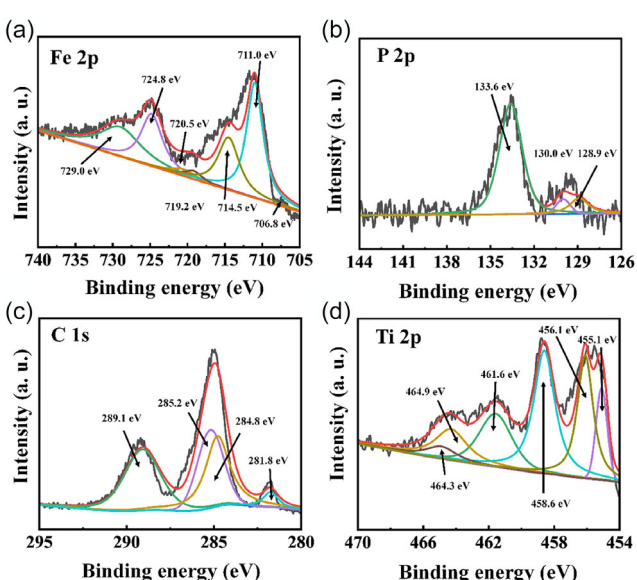


Figure 3. XPS spectra of $\text{FeP}_2@\text{Ti}_3\text{C}_2$: a) Fe 2p; b) P 2p; c) C 1s; and d) Ti 2p.

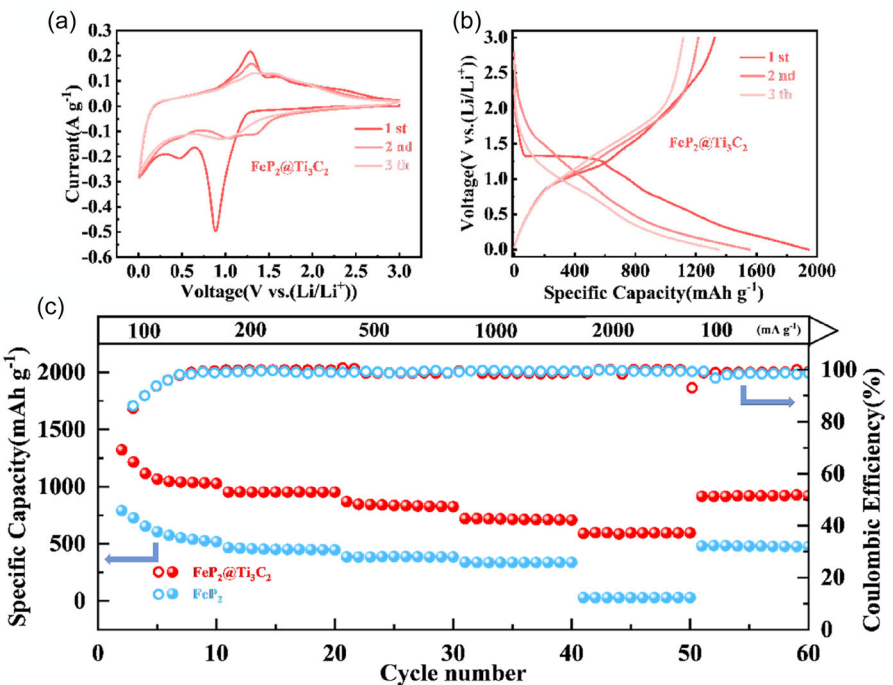


Figure 4. a) CV curves of the first three cycles of $\text{Li}||\text{FeP}_2@\text{Ti}_3\text{C}_2$ full batteries at 0.5 mV s^{-1} . b) Charge–discharge profiles of the first three cycles of $\text{Li}||\text{FeP}_2@\text{Ti}_3\text{C}_2$ batteries at 100 mA g^{-1} . c) Rate performance of $\text{Li}||\text{FeP}_2@\text{Ti}_3\text{C}_2$ and $\text{Li}||\text{FeP}_2$ batteries.

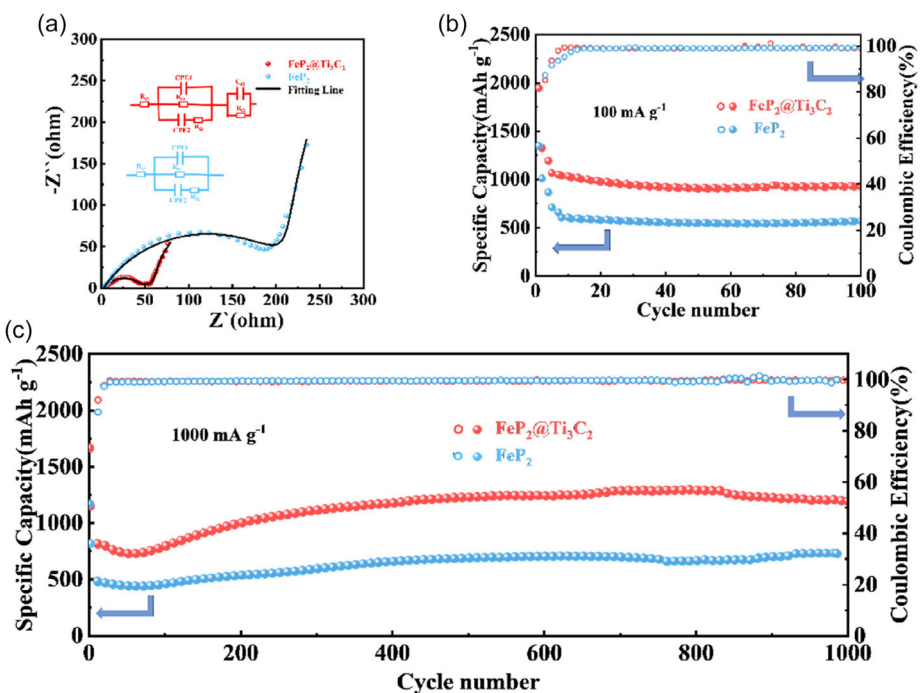


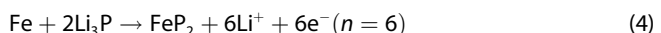
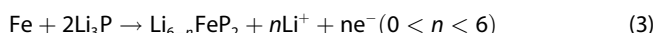
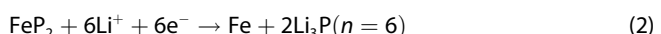
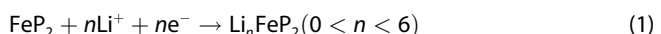
Figure 5. a) Nyquist plots of $\text{Li}||\text{FeP}_2@\text{Ti}_3\text{C}_2$ and $\text{Li}||\text{FeP}_2$ batteries. Cycling stability of $\text{Li}||\text{FeP}_2@\text{Ti}_3\text{C}_2$ and $\text{Li}||\text{FeP}_2$ batteries under b) 100 mA g^{-1} and c) 1000 mA g^{-1} .

number of active sites on the electrode surface. This enhancement contributes to improved battery capacity and reduced overall impedance. Figure 5b showed the cycling test of $\text{FeP}_2@\text{Ti}_3\text{C}_2$ at 100 mA g^{-1} , the first discharge reached 1965 mAh g^{-1} , and the

reversible specific capacity was still 938 mAh g^{-1} after 100 cycles. The reason for the decrease and then increase of the specific capacity was the joint result of the full contact between the electrolyte and the surface of $\text{FeP}_2@\text{Ti}_3\text{C}_2$. The generation of a stable

SEI film after many cycles, Figure 5c, showed the long cycling test of $\text{FeP}_2@\text{Ti}_3\text{C}_2$ at a current density of 1000 mA g^{-1} . $\text{FeP}_2@\text{Ti}_3\text{C}_2$ still possessed a specific capacity of 1194 mAh g^{-1} after 1000 cycles.

The kinetic analysis of $\text{FeP}_2@\text{Ti}_3\text{C}_2$ was performed and the results were shown in Figure 6. Compared with the CV curve of FeP_2 (Figure S5, Supporting Information) $\text{FeP}_2@\text{Ti}_3\text{C}_2$ at $0.5\text{--}6 \text{ mV s}^{-1}$ CV curves (Figure 6a), the peak position did not change much with the sweep speed, which indicated that the reversibility of $\text{FeP}_2@\text{Ti}_3\text{C}_2$ was more favorable. The reduction peaks at $0.31\text{--}0.59 \text{ V}$ indicate the lithiation during the binding of FeP_2 with Li^+ . (Equation (1), (2)). The oxidation peaks at $1.76\text{--}2.21 \text{ V}$ were because of the progressive delithiation reaction of Li_3P (Equation (3), (4)).^[56]



When the molar ratio of lithium to iron is less than 6, the primary product formed in this process is Li_nFeP_2 . Its crystal structure contains two iron sites and four phosphorus sites. During the lithiation process, the volume of FeP_2 increases, and the n value in Li_nFeP_2 continues to rise. The old covalent bonds between different iron and phosphorus sites break down, and new covalent bonds are formed between different sites.^[16,56,61] As the volume of FeP_2 increases, the interlayer spacing of the Ti_3C_2 layered structure also gradually increases, resulting in a larger contact area

with the electrolyte, which further facilitates the lithiation process and exhibits higher capacity.^[62,63,64] Figure 6b showed the b-value determined from the mathematical relationship between peak current and sweep speed, the b-value of the anodic peak of $\text{FeP}_2@\text{Ti}_3\text{C}_2$ was 0.627 and the b-value of the cathodic peak was 0.558, while the b-value of the FeP_2 anodic peak was 0.587 and the b-value of the cathodic peak was 0.501 (Figure S6, Supporting Information). It indicated that the composite battery behavior coexists with the capacitive property, and the introduction of Ti_3C_2 improved the capacitive behavior of FeP_2 . $\text{FeP}_2@\text{Ti}_3\text{C}_2$ at 0.5 mV s^{-1} had a significant improvement compared to the capacitance-controlled contribution of 62.7% at 0.5 mV s^{-1} for FeP_2 (Figure S7, Supporting Information), with a year-on-year 69% increase. To determine the b-value, the peak currents and corresponding scan rates from the CV curves measured at different scan rates were fitted to (Equation 5)

$$i = av^b \quad (5)$$

where i represents the peak current density and v represents the scan rate. At a specific scan rate, the data were fitted to (Equation 6) to obtain the parameters k_1 and k_2

$$i(v) = k_1v + k_2v^{0.5} \quad (6)$$

The resulting function was then integrated and compared with the integrated area of the original CV curve to calculate the ratio of the capacitive contribution. At each scan rate, the capacitive contribution ratio of $\text{FeP}_2@\text{Ti}_3\text{C}_2$ (Figure 6d) was higher than that of FeP_2 (Figure S8, Supporting Information), indicating that $\text{FeP}_2@\text{Ti}_3\text{C}_2$ exhibits faster reaction kinetics.^[65-69]

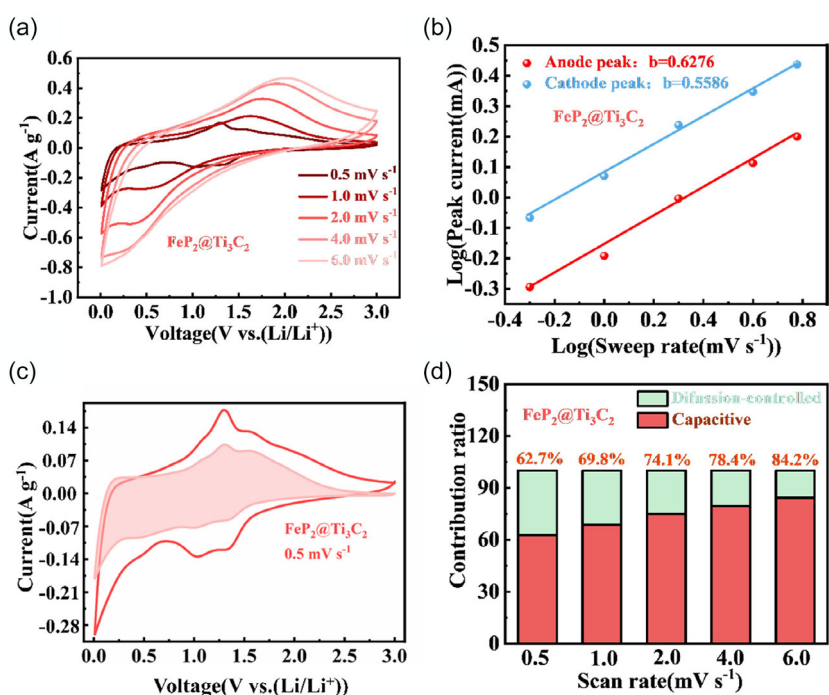


Figure 6. a) CV curves of $\text{Li}||\text{FeP}_2@\text{Ti}_3\text{C}_2$ batteries at different scan rates. b) Peak current and sweep rate fitting of $\text{FeP}_2@\text{Ti}_3\text{C}_2$. c) Capacitive contribution of $\text{FeP}_2@\text{Ti}_3\text{C}_2$ at 0.5 mV s^{-1} . d) Capacitive contribution ratio at different scan rates of $\text{FeP}_2@\text{Ti}_3\text{C}_2$.

3. Conclusions

The $\text{FeP}_2@\text{Ti}_3\text{C}_2$ is obtained by combining MXene with FeP_2 using a hydrothermal low-temperature phosphating method, and is successfully synthesized as confirmed by XRD and SEM tests. The FeP_2 on $\text{FeP}_2@\text{Ti}_3\text{C}_2$ is uniformly and firmly dispersed in the surface of the MXene layer structure. The introduction of MXene improves the conductivity of $\text{FeP}_2@\text{Ti}_3\text{C}_2$, reduces the interface resistance, and reduces the volume expansion and fragmentation of FeP_2 . Compared to FeP_2 , $\text{FeP}_2@\text{Ti}_3\text{C}_2$ has lower interface impedance, higher battery capacity, and better cycle life. After 1000 cycles, $\text{FeP}_2@\text{Ti}_3\text{C}_2$ still possesses a specific capacity of 1194 mAh g^{-1} . $\text{FeP}_2@\text{Ti}_3\text{C}_2$ provides a new approach to improving the performance of lithium-ion batteries.

4. Experimental Section

Synthesis of Ti_3C_2

Ti_3AlC_2 MAX (99%, (Ti 73.8 wt%, Al 13.86 wt%, C 12.34 wt%), Yiyi technology co., Ltd.) phase was used as the precursor, LiF (98.5%, Sinopharm Chemical Reagents Co., Ltd.) and HCl (Ar, Sinopharm Chemical Reagents Co., Ltd.) were used as etching agents to etch the precursor MAX. First, 9 mol L^{-1} HCl (40 mL) was measured in a vial of PTFE, and a small amount of 2.0 g of weighed LiF was added to it several times, and LiF was dissolved in hydrochloric acid solution by stirring for 20 min at room temperature, and a small amount of LiF was added to the dissolved LiF in hydrochloric acid solution several times. The precursor Ti_3AlC_2 MAX phase was added into the hydrochloric acid solution with LiF dissolved. After the reaction for 5 min, no gas was produced, the lid was put on, and the reactor was placed in a thermostatic water bath at 45 °C for 40 h. After the reaction, centrifugation and washing operation were performed, and the supernatant was washed with deionized water to a pH of 7. The precipitates were homogeneously mixed with 150 mL of deionized water, and a small amount of alcohol was added in order to aid in the stripping, which was ultrasonicated for 1 h under the protection of Ar. The concentration of the Ti_3C_4 dispersion used in the experiment was 20 mg mL^{-1} .

Synthesis of $\text{FeP}_2@\text{Ti}_3\text{C}_2$ -pro

First of all, 5 mL of Ti_3C_2 dispersion with 0.50 g ferrous oxalate (99%, Sinopharm Chemical Reagents Co., Ltd.) and 2 g $\text{CH}_4\text{N}_2\text{O}$ (99.5%, Sinopharm Chemical Reagents Co., Ltd.) were stirred in argon for 30 min, and then ultrasonicated for 30 min. The solution was added into 100 mL of polytetrafluoroethylene liner and reacted at 120 °C for 7 h. After cooling and being centrifugally washed for three times, it was put into the vacuum freeze drier for freeze-drying, resulting in $\text{FeP}_2@\text{Ti}_3\text{C}_2$ -pro.

Synthesis of $\text{FeP}_2@\text{Ti}_3\text{C}_2$

We took 0.1 g of $\text{FeP}_2@\text{Ti}_3\text{C}_2$ -pro in a porcelain boat, 2 g of sodium hypophosphite was taken in another porcelain boat, then the sodium hypophosphite and $\text{FeP}_2@\text{Ti}_3\text{C}_2$ -pro were placed upstream and downstream of the tube furnace, respectively. The temperature was increased to 330 °C at 3 °C min^{-1} for 2 h. The sample was taken out after the tube furnace was reduced to room temperature.

Material Characterization

The phase purity and crystal structure of the samples were characterized by XRD using a copper target $\text{K}\alpha$ radiation source ($\lambda = 1.54 \text{ \AA}$), operated at 40 kV and 100 mA. The diffraction data were collected over a 2θ range of 5–90°. Morphology and microstructure were examined using SEM at an accelerating voltage of 20 kV and TEM at an acceleration voltage of 80 kV. Surface chemical composition and binding energies were analyzed by XPS with a pass energy of 120 eV and a step size of 0.6 eV.

Preparation of Electrodes

The active material, conductive agent (Super P; 95%, Kejingzhida Co., Ltd.), and binder (PVDF; 98%, Kejingzhida Co., Ltd.) were weighed according to the ratio of 7:2:1, and stirred in the diluent (NMP; 98.5%, Kejingzhida Co., Ltd.) for 30 min. The stirred slurry was coated on the cleaned and dried abrasive surface of the copper foil with a coater, and then the pole piece was placed in a vacuum oven and dried at 60 °C for 12 h. When the moisture of the pole piece evaporated, the pole piece was cut into 12 mm diameter discs with a shear machine, and the mass of the pole piece and the surrounding uncoated copper foil were weighed and marked for use. After the moisture of the pole piece evaporated, the pole piece was cut into 12 mm diameter discs by shearing machine, weighed the mass of the pole piece and the mass of the uncoated copper foil around it, and then labeled and prepared for use.

Assembled Batteries

In the lithium-ion battery assembly, the prepared active materials were coated on the copper foil as the working electrode, polypropylene microporous membrane for lithium diaphragm, the use of lithium metal plate served both as the reference electrode and counter electrode, and 1.0 M LiPF_6 was dissolved in a mixture of EC: DMC: EMC = 1:1:1 vol% solution as the electrolyte solution used in this experiment. The process of assembling the battery was done in the glove box filled with high purity argon gas. The test requirements were water and oxygen content which were less than 0.5 ppm. When the assembly was completed, the unencapsulated battery was removed for compaction sealing and then tested for electrochemical performance test after 12 h of resting.

Electrochemical Measurements

The shape of the resulting CV performance curve was used to analyze the chemical reactions and their properties over the scanning range. EIS and CV tests were performed on the prepared cells using the Autolab electrochemical work. CV tests were carried out in the voltage range of 0.001–3 V with scan rates of 0.5, 1, 2, 4, and 6 mV s^{-1} . The batteries were subjected to 100 cycles at a current density of 100 mA g^{-1} using the NEWARE Battery Test System (BTS CT-4008); and ten cycles at multiplicative rates at current densities of 100, 200, 500, 1000, and 2000 mA g^{-1} , respectively.

Acknowledgements

This work was supported by the Science and Technology Program Joint Project of Liaoning Province (2024-BSLH-219), the Basic Scientific Research Project of The Education Department of

Liaoning Province (LJ212410149004, LJ222410149014), the Key Laboratory of Superlight Materials and Surface Technology, Ministry of Education, and the Fundamental Research Funds for the Central University of China (3072022JC0305).

Conflict of Interest

The authors declare no conflict of interest.

Author Contributions

Chenyi Yang: data curation (equal); methodology (equal); visualization (equal); writing—original draft (equal). **Wende Bai:** writing—review and editing (equal). **Zhe Gong:** data curation (equal); writing—original draft (equal); writing—review and editing (equal). **Zhuo Li:** writing—review and editing (equal). **Pengfei Wang:** writing—review and editing (equal). **Mingdong Zhou:** supervision (equal); writing—review and editing (equal). **Kai Zhu:** writing—review and editing (equal). **Chenyi Yang and Wende Bai** contributed equally to this work.

Data Availability Statement

The data that support the findings of this study are available from the corresponding author upon reasonable request.

Keywords: anodes · conducting materials · FeP₂ · lithium · MXene

- [1] P. Roy, S. K. Srivastava, *J. Mater. Chem. A* **2015**, *6*, 2454.
[2] B. Yang, Y. Wang, R. Zheng, W. Yang, Y. Li, T. Li, K. Li, A. Hu, J. Long, S. Ding, *Angew. Chem. Int. Ed.* **2025**, *64*, e202508486.
[3] T. Li, A. Hu, Y. Li, B. Yang, K. Li, K. Chen, J. Jiang, F. Li, Z. Seh, J. Wang, J. Long, *Adv. Funct. Mater.* **2025**, 2507310.
[4] R. Zhang, K. Zhu, J. Huang, L. Yang, S. Li, Z. Wang, J. Xie, H. Wang, J. Liu, *J. Alloy Compd.* **2019**, *755*, 490.
[5] K. Li, A. Hu, R. Xu, W. Xu, B. Yang, T. Li, Y. Li, Z. Seh, J. Long, S. Chen, *Adv. Energy Mater.* **2025**, *15*, 2501236.
[6] F. Yuan, C. Shi, Q. Li, J. Wang, D. Zhang, Q. Wang, H. Wang, Z. Li, W. Wang, B. Wang, *Adv. Funct. Mater.* **2022**, *32*, 2208966.
[7] J. Conzen, S. Lakshmi, A. Kapahi, S. Kraft, M. DiDomizio, *J. Loss Prev. Process Ind.* **2023**, *81*, 104932.
[8] K. Chen, A. Hu, G. Zhu, Y. Li, J. Jiang, B. Yang, T. Li, K. Li, J. Chen, W. Xu, Z. Wang, R. Xu, W. Yang, J. Wang, G. Wu, J. Long, Z. Seh, *ACS Nano* **2025**, *14*, 14284.
[9] C. Marion, L. Boulet, P. Gaveau, B. Fraisse, L. Monconduit, *J. Mater. Chem. A* **2012**, *22*, 22713.
[10] D. Sun, M. Wang, Z. Li, G. Fan, L. Fan, A. Zhou, *Electrochim. Commun.* **2014**, *47*, 80.
[11] Y. Guo, Y. Chang, L. Wang, Q. Xia, A. Zhou, *Surf. Interfaces* **2024**, *46*, 103986.
[12] R. Zhang, C. Zhang, W. Chen, *J. Mater. Chem. A* **2016**, *4*, 18723.
[13] J. Wang, J. Cui, Z. Li, D. Zhang, H. Sun, H. Wang, Q. Wang, H. J. Woo, S. Ramesh, W. Bo, *Chem. Eng. J.* **2023**, *464*, 142764.
[14] B. Wang, L. Yang, F. Yuan, D. Zhang, H. Wang, Q. Wang, H. Sun, Z. Li, H. Sun, W. Li, *Electrochim. Acta* **2023**, *439*, 141681.
[15] P. Veluri, S. Mitra, *RSC Adv.* **2016**, *6*, 87675.
[16] J. Jiang, W. Wang, C. Wang, L. Zhang, K. Tang, J. Zuo, Q. Yang, *Electrochim. Acta* **2015**, *170*, 140.
[17] P. Zhu, Z. Zhang, S. Hao, B. Zhang, P. Zhao, J. Yu, J. Cai, Y. Huang, Z. Yang, *Carbon* **2018**, *139*, 477.
[18] J. Jiang, C. Wang, J. Liang, J. Zhao, Q. Yang, *Dalton Trans.* **2015**, *44*, 10297.
[19] M. Zhang, J. Yu, T. Ying, J. Yu, Y. Sun, X. Liu, *J. Alloy Compd.* **2019**, *777*, 860.
[20] H. Jiang, B. Chen, J. Pan, C. Li, C. Liu, L. Liu, T. Yang, W. Li, H. Li, Y. Wang, L. Chen, M. Chen, *J. Alloy Compd.* **2017**, *728*, 328.
[21] H. Liu, C. Duan, C. Yang, W. Shen, F. Wang, Z. Zhu, *Sens. Actuators B: Chem.* **2015**, *218*, 60.
[22] X. Xie, Y. Xue, L. Li, S. Chen, Y. Nie, W. Ding, Z. Wei, *Nanoscale* **2014**, *6*, 11035.
[23] K. Zhang, D. Zhao, Z. Qian, X. Gu, J. Yang, Y. Qian, *Sci. China Mater.* **2023**, *66*, 51.
[24] W. Bao, X. Tang, X. Guo, S. Choi, C. Wang, Y. Gogotsi, G. Wang, *Joule* **2018**, *2*, 778.
[25] Y. Guo, D. Zhang, Y. Yang, Y. Wang, Z. Bai, P. Chu, Y. Luo, *Nanoscale* **2021**, *13*, 4624.
[26] X. Song, H. Wang, S. Jin, M. Lv, Y. Zhang, X. Kong, H. Hu, T. Ma, X. Luo, H. Tan, D. Hu, C. Deng, X. Chang, J. Xu, *Nano Res.* **2020**, *13*, 1659.
[27] X. Mao, Y. Zou, F. Xu, L. Sun, H. Chu, H. Zhang, J. Zhang, C. Xiang, *ACS Appl. Mater. Interfaces* **2021**, *13*, 22664.
[28] S. Yi, L. Wang, X. Zhang, C. Li, W. Liu, K. Wang, X. Sun, Y. Xu, Z. Yang, Y. Cao, J. Sun, Y. Ma, *Sci. Bull.* **2021**, *66*, 914.
[29] X. He, S. Jin, L. Miao, Y. Cai, Y. Hou, H. Li, K. Zhang, Z. Yan, J. Chen, *Angew. Chem. Int. Ed.* **2020**, *59*, 16705.
[30] J. Luo, W. Zhang, H. Yuan, C. Jin, L. Zhang, H. Huang, C. Liang, Y. Xia, J. Zhang, Y. Gan, X. Tao, *ACS Nano* **2017**, *11*, 2459.
[31] P. Huang, S. Zhang, H. Ying, W. Yang, J. Wang, R. Guo, W. Han, *Nano Res.* **2020**, *14*, 1218.
[32] J. Li, X. Yuan, C. Lin, Y. Yang, L. Xu, X. Du, J. Xie, J. Lin, J. Sun, *Adv. Energy Mater.* **2017**, *7*, 1602725.
[33] A. Levitt, M. Alhabeb, C. Hatter, A. Sarycheva, G. Dion, Y. Gogotsi, *J. Mater. Chem. A* **2019**, *7*, 269.
[34] X. Chen, Y. Zhu, M. Zhang, J. Sui, W. Peng, Y. Li, G. Zhang, F. Zhang, X. Fan, *ACS Nano* **2019**, *13*, 9449.
[35] Z. Chen, J. R. Dahn, *Electrochim. Acta* **2004**, *49*, 1079.
[36] F. Kong, C. Liang, L. Wang, Y. Zheng, S. Perananthan, R. C. Longo, J. P. Ferraris, M. Kim, K. Cho, *Adv. Energy Mater.* **2018**, *9*, 1802586.
[37] X. Ma, C. Ji, X. Yu, Y. Liu, X. Xiong, *ACS Appl. Mater. Interface* **2021**, *13*, 53965.
[38] H. Liang, H. N. Alshareef, *Small Methods* **2017**, *1*, 1700111.
[39] Z. Liang, R. Huo, S. Yin, F. Zhang, S. Xu, *J. Mater. Chem. A* **2014**, *2*, 921.
[40] Z. Li, L. Zhang, X. Ge, C. Li, S. Dong, C. Wang, L. Yin, *Nano Energy* **2017**, *32*, 494.
[41] P. Zhu, Z. Zhang, P. Zhao, B. Zhang, X. Cao, J. Yu, J. Cai, Y. Huang, Z. Yang, *Carbon* **2019**, *142*, 269.
[42] S. Zhang, D. Guan, Z. Xue, C. Shen, Y. Shen, G. Hu, Y. Cao, Z. Peng, W. Wang, Y. Ren, L. Kang, Z. Xue, K. Du, *Chem. Eng. J.* **2025**, *503*, 158219.
[43] F. Li, J. Gao, Z. He, N. Brandon, X. Li, L. Kong, *Energy Storage Mater.* **2022**, *48*, 20.
[44] Z. Liu, H. Peng, X. Xie, X. Wang, Y. Pu, G. Ma, Z. Lie, *J. Power Sources* **2022**, *543*, 231831.
[45] Y. Jiang, L. Zhao, H. Guo, C. An, M. Yue, C. Liu, Y. Wang, *J. Energy Storage* **2023**, *64*, 107146.
[46] J. Su, C. Zhang, X. Chen, S. Liu, T. Huang, A. Yu, *J. Power Sources* **2018**, *381*, 66.
[47] P. Guan, J. Li, T. Lu, T. Guan, Z. Ma, Z. Peng, X. Zhu, L. Zhang, *ACS Appl. Mater.* **2018**, *10*, 34283.
[48] R. Nava, L. Cremar, V. Agubra, J. Sanchez, M. Alcoutlabi, K. Lozano, *ACS Appl. Mater. Interfaces* **2016**, *8*, 29365.
[49] W. Yang, H. Ying, S. Zhang, R. Guo, J. Wang, W. Han, *Electrochim. Acta* **2020**, *337*, 135687.
[50] Z. Li, Z. Li, W. Zhong, C. Li, L. Li, H. Zhang, *Chem. Eng. J.* **2017**, *319*, 1.
[51] S. Zhao, X. Meng, K. Zhu, F. Du, G. Chen, Y. Wei, Y. Gogotsi, Y. Gao, *Energy Storage Mater.* **2017**, *8*, 42.
[52] W. Luo, Y. Liu, F. Li, J. Huo, D. Zhao, J. Zhu, S. Guo, *Appl. Surf. Sci.* **2020**, *523*, 146387.
[53] J. Zhou, S. Lin, Y. Huang, P. Tong, B. Zhao, X. Zhu, Y. Sun, *Chem. Eng. J.* **2019**, *373*, 203.
[54] S. Zhu, H. S. C. Wang, P. Zhang, P. Wan, X. Guo, Z. Yu, W. Wang, S. Chen, W. Chu, L. Song, *Adv. Mater.* **2021**, *34*, 2108809.
[55] C. Chen, X. Xie, B. Anasori, A. Sarycheva, T. Makaryan, M. Zhao, P. Urbankowski, L. Miao, J. Jiang, Y. Gogotsi, *Angew. Chem. Int. Ed.* **2018**, *57*, 1846.
[56] J. Liu, A. Wu, R. Tian, R. A. P. Camacho, S. Zhou, H. Huang, M. Yao, *Mater. Today Energy* **2020**, *18*, 100545.

- [57] H. Koh, S. J. Kim, K. Maleski, S. Cho, Y. Kim, C. Ahn, Y. Gogotsi, H. Jung, *ACS Sens.* **2019**, *4*, 1365.
- [58] S. N. Britvin, M. N. Murashko, Y. Vapnik, Y. S. Polekhovsky, S. V. Krivovichev, O. S. Vereshchagin, N. S. Vlasenko, V. V. Shilovskikh, A. N. Zaitsev, *Phys. Chem. Miner.* **2018**, *46*, 361.
- [59] J. W. Hall, N. Membreño, J. Wu, H. Celio, R. A. Jones, K. J. Stevenson, *J. Am. Chem. Soc.* **2012**, *134*, 5532.
- [60] X. Sha, X. Song, P. Gao, F. Zeng, Z. Wang, W. Zhou, X. Wu, M. Yu, Z. Shi, J. Liu, C. Jiang, *Nano Energy* **2025**, *144*, 111341.
- [61] Z. Li, Y. Wei, Y. Liu, S. Yan, M. Wu, *Adv. Sci.* **2023**, *10*, 2206860.
- [62] X. Li, X. Zhu, Z. Cao, Z. Xu, J. Shen, M. Ye, *Small* **2021**, *18*, 2105325.
- [63] T. He, X. Kang, F. Wang, J. Zhang, T. Zhang, F. Ran, *Mat. Sci. Eng. R: Rep.* **2023**, *154*, 100737.
- [64] L. Guan, L. Yu, G. Z. Chen, *Electrochim. Acta* **2016**, *206*, 464.
- [65] Y. Gogotsi, R. M. Penner, *ACS Nano* **2018**, *12*, 2081.
- [66] B. Evanko, S. W. Boettcher, S. J. Yoo, G. D. Stucky, *ACS Energy Lett.* **2017**, *2*, 2581.
- [67] Y. Jiang, J. Liu, *Energy Environ. Mater.* **2019**, *2*, 30.
- [68] Y. Ma, X. Wang, H. Yuan, G. Chang, J. Zhu, H. Dai, X. Wei, *Renewable Sustainable Energ. Rev.* **2025**, *211*, 115226.
- [69] A. Maradesa, B. Py, J. Huang, Y. Lu, P. Iurillr, A. Mrozinski, H. M. Law, Y. Wang, Z. Wang, J. Li, S. Xu, Q. Meyer, J. Liu, C. Brivio, A. Gavrilyuk, K. Kobayashi, A. Bertei, N. J. Williams, C. Zhao, M. Danzer, F. Ciucci, *Joule* **2024**, *8*, 1958.

Manuscript received: July 3, 2025

Revised manuscript received: August 25, 2025

Version of record online:
